



# Numerical Simulations of an Initially Top-hat Jet and the Afterglow of GW170817/GRB170817A

Ramandeep Gill<sup>1,2</sup>, Jonathan Granot<sup>1,3</sup>, Fabio De Colle<sup>4</sup>, and Gerardo Urrutia<sup>4</sup><sup>1</sup> Department of Natural Sciences, The Open University of Israel, P.O. Box 808, Ra'anana 43537, Israel<sup>2</sup> Physics Department, Ben-Gurion University, P.O. Box 653, Beer-Sheva 84105, Israel<sup>3</sup> Department of Physics, The George Washington University, Washington, DC 20052, USA<sup>4</sup> Instituto de Ciencias Nucleares, Universidad Nacional Autónoma de México, A.P. 70-543 04510 D.F., Mexico

Received 2019 February 26; revised 2019 July 23; accepted 2019 July 23; published 2019 September 17

## Abstract

The afterglow of GRB 170817A/GW170817 was very unusual, slowly rising as  $F_\nu \propto t_{\text{obs}}^{0.8} \nu^{-0.6}$ , peaking at  $t_{\text{obs, pk}} \sim 150$  days, and sharply decaying as  $\sim t_{\text{obs}}^{-2.2}$ . Very-long-baseline interferometry observations revealed an unresolved radio afterglow image whose flux centroid apparently moved superluminally with  $v_{\text{app}} \approx 4c$  between 75 and 230 days, clearly indicating that the afterglow was dominated by a relativistic jet's compact core. Different jet angular structures successfully explained the afterglow light curves: Gaussian and steep power-law profiles with narrow core angles  $\theta_c \lesssim 5^\circ$  and significantly larger viewing angles  $\theta_{\text{obs}}/\theta_c \sim 3-5$ . However, a top-hat jet (THJ; conical with sharp edges at  $\theta = \theta_0$ ) was ruled out because it appeared to produce an early flux rise much steeper ( $\propto t_{\text{obs}}^a$  with  $a \gtrsim 3$ ) than observed. Using 2D relativistic hydrodynamic simulations of an initially THJ, we show that the initial steep flux rise is an artifact caused by the simulation's finite start time,  $t_0$ , missing its flux contributions from  $t < t_0$  and sometimes "compensated" using an analytic THJ. While an initially THJ is not very physical, such simulations are particularly useful at  $t_{\text{obs}} \gtrsim t_{\text{obs, pk}}$  when the afterglow emission is dominated by the jet's core and becomes insensitive to its exact initial angular profile if it drops off sharply outside of the core. We demonstrate that an initially THJ fits GW170817/GRB 170817A's afterglow light curves and flux centroid motion at  $t_{\text{obs}} \gtrsim t_{\text{obs, pk}}$ , for  $\theta_{\text{obs}}/\theta_0 \approx 3$  and may also fit the earlier light curves for  $\Gamma_0 = \Gamma(t_0) \gtrsim 10^{2.5}$ . We analytically express the degeneracies between the model parameters, and find a minimal jet energy of  $E_{\text{min}} \approx 5.3 \times 10^{48}$  erg and circumburst medium density of  $n_{\text{min}} \approx 5.3 \times 10^{-6} \text{ cm}^{-3}$ .

**Key words:** gamma-ray burst: general – gravitational waves – hydrodynamics – ISM: jets and outflows – methods: numerical – relativistic processes

## 1. Introduction

The first gravitational wave (GW) detection of a binary neutron star merger, GW170817 (Abbott et al. 2017a), was accompanied by the first electromagnetic counterpart to any GW detection—the weak, short duration gamma-ray burst, GRB 170817A (Abbott et al. 2017b), that originated in the nearby ( $D \approx 40$  Mpc) elliptical galaxy NGC 4993 (Coulter et al. 2017). An impressive observational campaign detected the quasi-thermal kilonova emission in the near-IR–optical–ultraviolet energy bands over the next few weeks (see, e.g., Abbott et al. 2017c, and references therein). The nonthermal afterglow emission was detected after 8.9 days in X-rays (Troja et al. 2017) and after 16.4 days in the radio (Hallinan et al. 2017).

GW170817/GRB 170817A's long-lived X-ray to radio afterglow emission was highly unusual. In contrast to the flux decay seen in almost all GRB afterglows, it showed an exceptionally long-lasting flux rise, as  $F_\nu(t_{\text{obs}}) \propto \nu^{-0.6} t_{\text{obs}}^{0.8}$ , up to the peak at  $t_{\text{obs, pk}} \sim 150$  days post merger (e.g., Margutti et al. 2018; Mooley et al. 2018b), followed by a sharp decay as  $F_\nu \propto t_{\text{obs}}^a$  where  $a \simeq -2.2$  (Mooley et al. 2018a; van Eerten et al. 2018). The broadband (X-rays, radio, and late-time optical) afterglow emission is consistent with arising from a single power-law segment (PLS) of the afterglow synchrotron spectrum,  $\nu_m \leq \nu \leq \nu_c$ .<sup>5</sup>

Almost all successful off-axis jet models for this afterglow have an angular profile that is either a (quasi-)Gaussian or a narrow core with sharp power-law wings (Troja et al. 2017, 2018; D'Avanzo et al. 2018; Gill & Granot 2018; Lamb & Kobayashi 2018; Lazzati et al. 2018; Margutti et al. 2018; Resmi et al. 2018). Moreover, several works have argued that a top-hat jet (THJ) can be ruled out (e.g., Margutti et al. 2018; Mooley et al. 2018b) as it would produce a very sharp initial flux rise ( $F_\nu \propto t_{\text{obs}}^a$  with  $a \gtrsim 3$ ) compared to the observed one. Such a sharp initial flux rise was obtained both numerically from 2D hydrodynamic simulations (e.g., van Eerten & MacFadyen 2011; Granot et al. 2018a), and analytically assuming an idealized THJ (e.g., Granot et al. 2002; Eichler & Granot 2006; Nakar & Piran 2018).

Here we show that while an idealized THJ would indeed produce sharply rising early light curves for off-axis observers, a more realistic description of the dynamics (using numerical simulations) for an initially THJ leads to a much shallower flux rise that can potentially explain the GRB 170817A afterglow observations (light curves, flux centroid motion, and upper limits on the image size). The main difference arises because within the simulation's first dynamical time an initial THJ develops a bow-shock like angular structure, which produces afterglow emission resembling that from a core-dominated structured jet,<sup>6</sup> with a much shallower flux rise, making the two models practically indistinguishable at  $t_{\text{obs}} \gtrsim t_{\text{obs, pk}}$ , and not

<sup>5</sup> Here,  $\nu_m$  is the synchrotron frequency of minimal energy electrons and  $\nu_c$  of electrons that cool on the dynamical time (Sari et al. 1998).

<sup>6</sup> I.e., a jet in which most of the energy resides within a narrow core, outside of which the energy per solid angle sharply drops.

always that easy to distinguish between even at earlier times. Numerical simulations have a finite lab-frame start time,  $t = t_0 > 0$ , thus missing contributions to  $F_\nu$  from  $t < t_0$ . This is often compensated for by adding emission at  $t < t_0$  from a conical wedge from the Blandford & McKee (1976, hereafter BM76) spherical self-similar solution (e.g., De Colle et al. 2012a, 2012b; van Eerten et al. 2012; Bietenholz et al. 2014; Granot et al. 2018a, 2018b). This still results in an unphysically sharp flux rise at early observed times,  $t_{\text{obs}} \lesssim 2t_{\text{obs},0}$ , corresponding to lab-frame times  $t \lesssim 2t_0$ .

The effects of  $t_0$  including  $t_{\text{obs},0}(\theta_{\text{obs}}, t_0)$  are analytically explained in Section 2. The effect of starting the simulations with a larger Lorentz factor (LF)  $\Gamma_0 = \Gamma(t_0)$  and correspondingly smaller  $t_0$  is shown in Section 3 through 2D relativistic hydrodynamic simulations. In Section 4 model scalings and the minimal energy and circumburst medium (CBM) density estimates are provided. In Section 5 we calculate and compare the flux centroid location and the image size and shape with radio afterglow measurements of GW170817/GRB 170817A. Our conclusions are discussed in Section 6.

## 2. The Effect of Simulation Start Time

We perform 2D relativistic hydrodynamical simulations with initial conditions of a conical wedge of half-opening angle  $\theta_0$  taken out of the BM76 solution. This initially narrow and relativistic jet expands into a cold CBM with a power-law rest-mass density profile with radius  $R$  from the central source,  $\rho(R) = AR^{-k}$ , where for uniform (wind-like) density environment  $k = 0$  ( $k = 2$ ). The BM76 spherical self-similar phase occurs after the original outflow is significantly decelerated and most of the energy is in the shocked CBM behind the forward (afterglow) shock. The material just behind the shock moves with velocity  $\beta c$ , with  $c$  being the speed of light, and bulk LF  $\Gamma = (1 - \beta^2)^{-1/2} = \Gamma_{\text{shock}}/\sqrt{2}$ . The BM76 phase reasonably holds for a THJ while  $\Gamma > 1/\theta_0$  (assuming  $\Gamma_0\theta_0 \gg 1$ , as typically inferred for GRBs) before significant lateral spreading can occur.

The radial width behind the forward shock containing most of the blastwave's energy is  $\Delta \sim 0.1 R/\Gamma^2$ . During the BM76 self-similar phase  $\Gamma^2 R^{3-k} = \Gamma_0^2 R_0^{3-k} = (17 - 4k)E_{k,\text{iso}}/16\pi Ac^2 = \text{const}$ , with  $R_0 = R(t_0) \approx ct_0$  being the initial shock radius. Thus the initial radial width  $\Delta_0 = \Delta(t_0) \sim 0.1R_0/\Gamma_0^2 \propto R_0^{4-k} \propto \Gamma_0^{-2(4-k)/(3-k)} (\propto \Gamma_0^{-8/3}$  for  $k = 0$ ) becomes much narrower and harder to resolve for larger  $\Gamma_0$  or correspondingly smaller  $t_0 \approx R_0/c \propto \Gamma_0^{-2/(3-k)} (\propto \Gamma_0^{-2/3}$  for  $k = 0$ ). This practically limits  $\Gamma_0$  from above and  $t_0$  from below.

An on-axis observer ( $\theta_{\text{obs}} < \theta_0$ ) receives the first photons from the simulation after a radial time delay of

$$\frac{t_{\text{obs},r}}{(1+z)} = t_0 - \frac{R_0}{c} \approx \frac{R_0}{4(4-k)c\Gamma_0^2} \approx \frac{t_0}{4(4-k)\Gamma_0^2}, \quad (1)$$

with  $z$  being the source's cosmological redshift. For an off-axis observer ( $\Delta\theta \equiv \theta_{\text{obs}} - \theta_0 > 0$ ), there is an additional angular time delay,

$$\begin{aligned} \frac{t_{\text{obs},\theta}}{(1+z)} &= \frac{R_0}{c} [1 - \cos(\Delta\theta)] \approx \frac{\Delta\theta^2}{2} t_0 \\ &\approx \frac{\Delta\theta^2}{2} \left[ \frac{(17-4k)E_{k,\text{iso}}}{16\pi Ac^{5-k}\Gamma_0^2} \right]^{\frac{1}{3-k}}, \end{aligned} \quad (2)$$

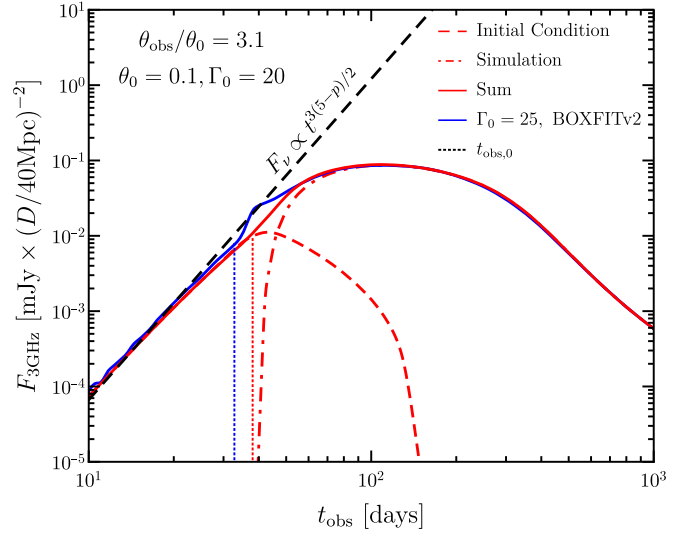


**Figure 1.** Simulated light-curve decomposition into the synthetic part, obtained from the initial condition (top-hat jet; THJ), and that obtained from the simulated region for  $t_{\text{obs}} > t_{\text{obs},0}$ . Comparison is made with the light curve from BOXFITv2 code ( $\Gamma_0 = 25$ ) for the same model parameters (see Figure 2). Extension of both light curves at  $t_{\text{obs}} < t_{\text{obs},0}$  matches the analytical flux scaling for an off-axis relativistic THJ (the slightly shallower slope toward  $t_{\text{obs},0}$  arises because of its proximity to  $t_{\text{obs},\text{pk}}$ ).

(e.g., Granot et al. 2017), which dominates the total time delay  $t_{\text{obs},0} = t_{\text{obs},r} + t_{\text{obs},\theta} \approx t_{\text{obs},\theta}$  for  $\Delta\theta > 1/\Gamma_0$ . For such off-axis viewing angles one can conveniently express  $\Gamma_0 \propto t_{\text{obs},0}^{-(3-k)/2}$ , which for  $k = 0$ ,  $E_{k,\text{iso}} \approx (2/\theta_0^2)E$  and  $z \ll 1$  gives

$$\begin{aligned} \Gamma_0 &\approx \sqrt{\frac{17E\theta_0^{-2}(\Delta\theta)^6}{64\pi n m_p c^5 t_{\text{obs},0}^3}} \\ &= 149 E_{50.3}^{1/2} n_{-3.6}^{-1/2} \theta_{0,-1}^{-1} \left( \frac{\Delta\theta}{0.21} \right)^3 \left( \frac{t_{\text{obs},0}}{10 \text{ days}} \right)^{-3/2}, \end{aligned} \quad (3)$$

where for the numerical value we normalize by our best-fit model parameters derived in Section 3, for which  $t_{\text{obs},0} = 38.1, 23.0, 18.3$  days for  $\Gamma_0 = 20, 40, 60$ .

The compactness argument implies that GRB jets typically have  $\Gamma_0 \gtrsim 100$  for the emission region to be optically thin to  $\gamma\gamma$ -annihilation (e.g., Lithwick & Sari 2001). Such large  $\Gamma_0$  are very difficult to simulate, and current numerical works usually set  $\Gamma_0 \sim 20$ –25 (see, however, van Eerten & MacFadyen 2013).

Simulations initialized at  $t_0$  do not contribute any flux at  $t_{\text{obs}} < t_{\text{obs},0}$  (see Figure 1). Over the first dynamical time ( $t_0 < t \lesssim 2t_0$ ), as the simulated jet relaxes from its artificially sharp top-hat initial condition, the flux sharply rises at times  $t_{\text{obs},0} \leq t_{\text{obs}} \lesssim 2t_{\text{obs},0}$ , after which the flux evolves smoothly with time. During this relaxation phase, the THJ is slowed down due to its interaction with the CBM and develops a bow-shock like structure (e.g., Granot et al. 2001; van Eerten & MacFadyen 2011; De Colle et al. 2012b). Its structure at this point resembles a “structured jet” with a highly energetic core, whose velocity is almost radial, surrounded by less energetic slower-moving material whose velocity points more sideways. Therefore, an initially THJ inevitably transforms into a structured jet. The slower material at angles  $\theta > \theta_0$  has a much wider beaming cone and its emission starts dominating the off-axis flux. As the jet gradually decelerates, its beaming

cone widens and off-axis observers start to receive flux from smaller  $\theta$  closer to the jet's core, resulting in a more gradual flux rise compared to an analytic perpetually sharp-edged jet.

To compensate for the missing flux at  $t_{\text{obs}} < t_{\text{obs},0}$ , as shown in Figure 1, light curves derived from numerical simulations are often supplemented with synthetic light curves obtained for the initial conditions (usually a conical wedge from the BM76 self-similar solution, e.g., De Colle et al. 2012a, 2012b; van Eerten et al. 2012; Bietenholz et al. 2014; Granot et al. 2018a, 2018b) over a wide range of earlier lab-frame times,  $t_* < t < t_0$  with  $t_* \ll t_0$ . We also compare the light curve obtained from the publicly available afterglow modeling code BOXFITv2 (van Eerten et al. 2012), which has been widely used to fit afterglow observations of GRB 170817A. Light curves obtained from our numerical simulations are in excellent agreement with that obtained from BOXFITv2.

The observed flux density is given by (e.g., Granot 2005; Granot & Ramirez-Ruiz 2012)

$$F_\nu(t_{\text{obs}}) = \frac{(1+z)}{4\pi d_L^2(z)} \int dt \delta_t \int \delta_D^3 dL'_{\nu'} \propto \delta_D^3 L'_{\nu'}, \quad (4)$$

where  $d_L(z)$  is the luminosity distance, the  $\delta$ -function,  $\delta_t = \delta(t - t_{\text{obs}}/(1+z) - R\tilde{\mu}/c)$ , accounts for the photon arrival times (Granot et al. 1999),  $R\tilde{\mu} = \hat{n} \cdot \mathbf{R}$  (Eichler & Waxman 2005) where  $\hat{n}$  is the direction to the observer, and  $\mathbf{R}$  is the radius vector (measured from the central source) of each fluid element having velocity  $\mathbf{v} = \beta c$  and Doppler factor  $\delta_D = [\Gamma(1 - \hat{n} \cdot \beta)]^{-1}$ . For radial velocities (e.g., a spherical shell),  $\hat{n} \cdot \beta = \beta\tilde{\mu}$  and  $\delta_D \approx 2\Gamma/[1 + (\Gamma\tilde{\mu})^2]$  for  $\Gamma \gg 1$ . In Equation (4),  $F_\nu \propto \delta_D^3 L'_{\nu'}$  holds where  $L'_{\nu'}$  and  $\delta_D$  are those of the part of the source that dominates the observed emission, which for a THJ viewed off-axis is within an angle  $\sim \max(\Gamma^{-1}, \Delta\theta)$  of the point in the jet closest to the observer (where  $\tilde{\theta} \approx \Delta\theta$ ), occupying a solid angle  $\Omega_* \sim \min[\max(\Gamma^{-2}, \Delta\theta^2), \theta_0^2]$ . During the early flux-rising phase while the radiation is beamed away from the observer ( $\Gamma > 1/\Delta\theta$ ),  $\Omega_* = \text{const}$  and one can use the scalings of  $L'_{\nu'}$  for a spherical flow,  $L'_{\nu'} \propto R^{a\nu'^b} \propto R^a \delta_D^{-b}$ , where the PLS-dependent power-law indices  $a$  and  $b$  are explicitly calculated in Granot (2005). Therefore,  $F_\nu \propto \delta_D^{3-b} R^a$  where (e.g., Salmonson 2003; Granot 2005)  $\delta_D \approx 2/\Gamma\Delta\theta^2 \propto R^{(3-k)/2} \implies F_\nu \propto R^{[2a+(3-k)(3-b)]/2}$ . For GRB 170817A, PLS G is relevant and  $a = [15 - 9p - 2k(3-p)]/4$ ,  $b = (1-p)/2$ . From Equation (2),  $t_{\text{obs}} \propto R$  which implies  $F_\nu \propto t_{\text{obs}}^{3(5-p)/2}$  for a uniform CBM ( $k=0$ ).

In Figure 1, we show the extension of the light curve to  $t_{\text{obs}} < t_{\text{obs},0}$ , where we reproduce the analytic flux scaling derived above. It is clear that BOXFITv2 also supplements the light curve at early times ( $t < t_0 \Leftrightarrow t_{\text{obs}} < t_{\text{obs},0}$ ) with the flux from a conical wedge out of the BM76 self-similar solution (also used for the initial conditions). Although BOXFITv2 allows the user to not include this extension in the final light curve, many works indeed do include it, even when fitting to observations. Either way, the flux at  $t_{\text{obs}} \lesssim 2t_{\text{obs},0}$  is strongly affected by the rather arbitrary simulation start time  $t_0$ . Initializing the simulation at a smaller  $t_0$  corresponding to a larger  $\Gamma_0$  would shift this feature to earlier times and recover the much shallower flux rise in the light curve.

### 3. Different $\Gamma_0$ Fits to the Afterglow Data of GW170817/GRB 170817A

Here we show results of 2D hydrodynamic simulations using the special-relativistic hydrodynamics code *Mezcal*, post-processed by a complimentary radiation code (see De Colle et al. 2012a, 2012b, for details). The simulations are initialized with a conical wedge of half-opening angle  $\theta_0 = 0.1, 0.2$  rad and initial LF  $\Gamma_0 = 20, 40, 60$  expanding into a uniform CBM ( $k=0$ ) of rest-mass density  $\rho_0 = nm_p$  and number density  $n$ ,  $m_p$  being the proton mass. The outflow has an isotropic-equivalent kinetic energy  $E_{k,\text{iso}} = 10^{53}$  erg, corresponding to a true jet energy of  $E = (1 - \cos\theta_0)E_{k,\text{iso}} \approx 5 \times 10^{50}$  erg for  $\theta_0 = 0.1$  and  $E \approx 2 \times 10^{51}$  erg for  $\theta_0 = 0.2$ .

We consider synchrotron radiation from relativistic electrons that are accelerated at the afterglow shock to a power-law energy distribution,  $dN_e/d\gamma_e \propto \gamma_e^{-p}$  for  $\gamma_e > \gamma_m$  with  $p = 2.16$ , which are a fraction  $\xi_e$  of all post-shock electrons, and hold a fraction  $\epsilon_e = 0.1$  of the post-shock internal energy density, where a fraction  $\epsilon_B = 0.1$  goes to the magnetic field. The radiation is calculated numerically for a fixed set of model parameters ( $E, n, \epsilon_e, \epsilon_B, p, \theta_0$ ) and for a grid of  $\theta_{\text{obs}}$  values. When including the parameter  $\xi_e$ , the set of model parameters become degenerate, where the afterglow flux is invariant under the change  $E \rightarrow E/\xi_e$ ,  $n \rightarrow n/\xi_e$ ,  $\epsilon_e \rightarrow \epsilon_e \xi_e$ , and  $\epsilon_B \rightarrow \epsilon_B \xi_e$ , for  $m_e/m_p < \xi_e \leq 1$ . We then use the scaling relations described in Granot (2012) for arbitrary values of ( $E, n$ ), as well as the scaling with the shock microphysical parameters in each PLS (Table 2 of Granot & Sari 2002). See Granot et al. (2018b) for further details.

There are in total eight model parameters, i.e.,  $E, n, \epsilon_e, \epsilon_B, p, \xi_e, \theta_0, \theta_{\text{obs}}$ . There are five effective observational constraints: (i) the spectral index  $b \approx -0.58$  ( $F_\nu \propto \nu^b$ ;  $b = [1-p]/2$  for PLS G, which determines  $p = 1-2b \approx 2.16$ ), (ii) the light-curve peak time  $t_{\text{obs,pk}} \approx 150$  days, (iii) the peak flux  $F_{\nu,\text{pk}}$ , (iv) the shape of the light curve near the peak (which approximately determines  $\theta_{\text{obs}}/\theta_0$ ), (v) the radio flux centroid's apparent velocity. These five constraints involve equalities and reduce the dimensionality of the allowed parameter space from an 8D to a 3D. There are also three additional constraints that involve inequalities and hence only reduce its volume but not its dimensionality: the fact that all the broadband afterglow observations lie within PLS G,  $\nu_m < \nu < \nu_c$ , and  $\theta_{\text{obs}} \lesssim 0.5$  from the GW detection.

Our afterglow light-curve fitting is guided by the measured peak at  $t_{\text{obs,pk}} \sim 150$  days (Dobie et al. 2018) and the data points near the peak. Figure 2 shows the fit to the afterglow data for different initial  $\Gamma_0$  (top-left panel) and viewing angles  $\theta_{\text{obs}}$  (top-right panel). We do not attempt to fit the early time data at  $t_{\text{obs}} \lesssim 40$  days, before the simulated light curves contain the dominant and dynamically relaxed contribution from the hydrodynamic simulation. Nevertheless, we obtain a reasonable fit to the afterglow data for different values of  $\Gamma_0$ , where our light curves for larger  $\Gamma_0$  extend to earlier times and can broadly explain the data at  $t_{\text{obs}} \gtrsim 40$  days.

The best constrained parameters are (also see Granot et al. 2018b): (i)  $p \approx 2.16$ , and (ii)  $\theta_{\text{obs}}/\theta_0 \approx 3.1 \pm 0.1$ , as it significantly affects the shape of the light curve before and around the peak time. In the bottom-right panel of Figure 2, we compare the model light curves for  $\theta_0 = 0.1, 0.2$  and show that in both cases  $\theta_{\text{obs}}/\theta_0 = 3.1$  provides a comparably good fit, while fixing the same values for the shock microphysical

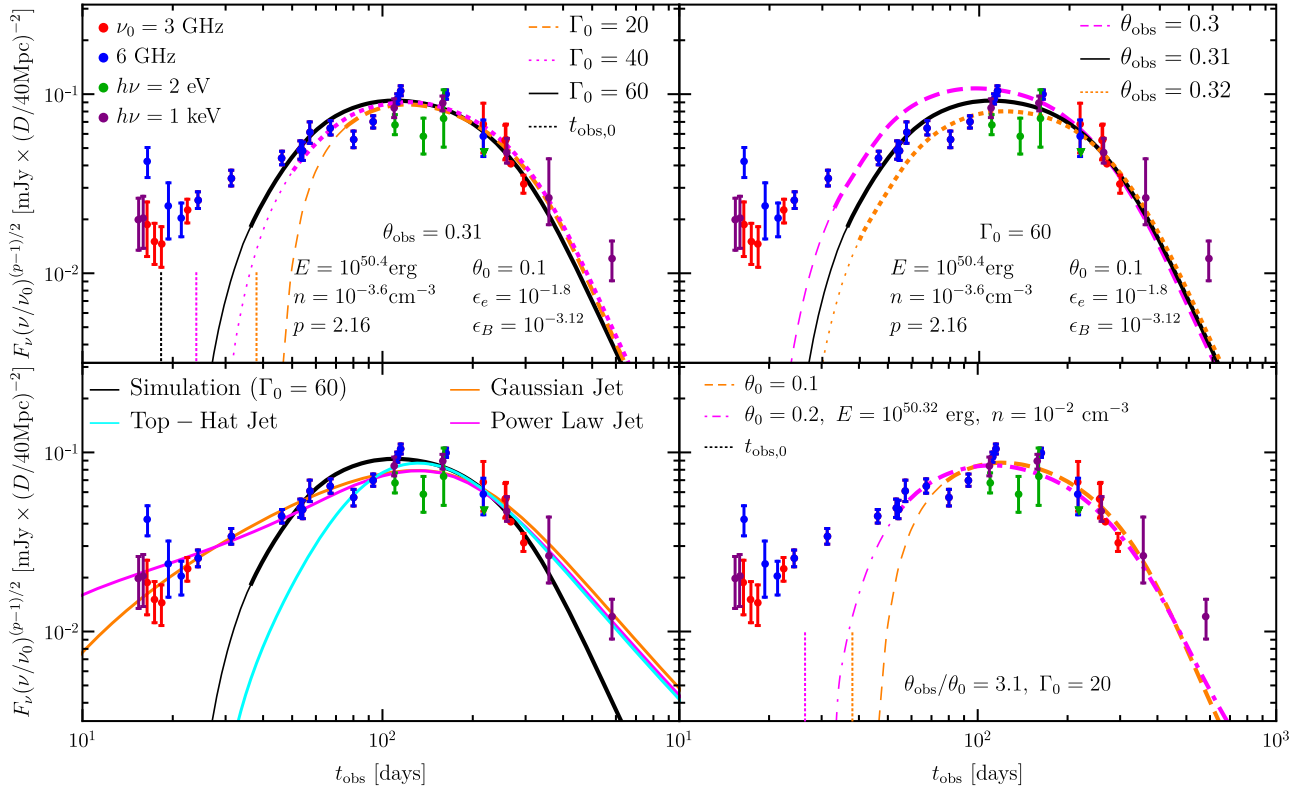


**Figure 2.** Comparison of simulated afterglow light curves for an initially THJ with observations, for different  $\Gamma_0$  (top-left), slightly different viewing angles  $\theta_{\text{obs}}$  (top-right), different  $\theta_0$  (bottom-right), and semi-analytic models of different jet structures (bottom-left; see text for model parameters). Observations in different energy bands (with late-time X-ray data from Haggard et al. 2018; Hajela et al. 2019) are normalized to the corresponding flux density at  $\nu_0 = 3$  GHz. Upper limits are marked by downward triangles. The simulated-flux deficiency at  $t_{\text{obs}} \lesssim 2t_{\text{obs},0}$  is an artefact of starting the simulation with low  $\Gamma_0$  and at a correspondingly large lab-frame time  $t_0$ . No simulation flux is available at  $t < t_0 \Leftrightarrow t_{\text{obs}} < t_{\text{obs},0}$ .

parameters but varying the true jet energy  $E$  and CBM density  $n$ .

We compare the simulation light curves with those obtained from semi-analytic models of different jet structures, namely a THJ, Gaussian jet (GJ), and a power-law jet (PLJ; see Gill & Granot 2018, for models of structured jets). For the THJ we prescribe the same dynamics as that for the two structured jets, i.e., every part of the jet evolves locally as if it were part of a spherical flow, with no sideways spreading. As a result, all three semi-analytic models yield very similar light curves right after the peak when the compact core of the jet becomes visible to the off-axis observer. On the other hand, the simplified dynamics of the semi-analytic models leads to a significantly shallower post-peak flux decay rate compared to the simulated one, which may be attributed to the combination of a shallower asymptotic decay and a smaller overshoot just after the peak (e.g., Granot 2007). The post-peak flux decay behavior of different structured jets will be investigated in more detail using 2D numerical simulations in another work (G. Urrutia et al. 2019, in preparation). For the semi-analytic models one set of model parameter values that can explain the observations sufficiently well are:  $E_{\text{k,iso,[c,jet]}} \approx 10^{51.6}$  erg,  $\theta_{\text{[c,jet]}} \approx 5^\circ$ ,  $\theta_{\text{obs}} = 27^\circ$ ,  $\epsilon_e \approx 10^{-1}$ ,  $\epsilon_B \approx 10^{-2.8}$ , and the only difference is in the core LFs between the three models, with  $\Gamma_c^{\text{PLJ}} = 100$ ,  $\Gamma_{\text{jet}}^{\text{THJ}} = \Gamma_c^{\text{GJ}} = 600$ .

#### 4. Flux Scalings, Model Degeneracies, and Minimum Jet Energy and CBM Density Estimates

For the light-curve fits we assume  $\xi_e = 1$ , and use the dependence on the shock microphysical parameters in PLS G

from Granot & Sari (2002), now including the degeneracy due to  $\xi_e$  (e.g., Eichler & Waxman 2005, van Eerten & MacFadyen 2012),  $F_{\nu,G} \propto \epsilon_e^{p-1} \epsilon_B^{(p+1)/4} \xi_e^{2-p} \nu^{(1-p)/2}$ . We also use the global scaling relations (Granot 2012), which are conveniently parameterized through length and time,

$$\alpha = \frac{\ell'}{\ell} = \frac{t'}{t} = \frac{t'_{\text{obs}}}{t_{\text{obs}}} = \left( \frac{E'/E}{n'/n} \right)^{1/3}, \quad (5)$$

and through mass and energy,  $\zeta = m'/m = E'/E$ , where the rescaled parameters are denoted with a prime,  $\mathcal{F} = F'_{\nu,G}(t'_{\text{obs}}, \epsilon'_e, \epsilon'_B, \xi'_e) / F_{\nu,G}(t_{\text{obs}}, \epsilon_e, \epsilon_B, \xi_e)$ ,

$$\mathcal{F} = \zeta^{\frac{(p+5)}{4}} \alpha^{-\frac{3(p+1)}{4}} \left( \frac{\epsilon'_e}{\epsilon_e} \right)^{p-1} \left( \frac{\epsilon'_B}{\epsilon_B} \right)^{\frac{(p+1)}{4}} \left( \frac{\xi'_e}{\xi_e} \right)^{2-p}. \quad (6)$$

Next, we constrain  $E$  from below by using these scaling relations and our (partly degenerate) best-fit parameters:  $E = 10^{50.4}$  erg,  $n = 10^{-3.6} \text{ cm}^{-3}$ ,  $\epsilon_e = 10^{-1.8}$ ,  $\epsilon_B = 10^{-3.12}$ ,  $\theta_{\text{obs}}/\theta_0 = 3.1$  (fixing  $\xi_e = 1$ ,  $p = 2.16$ ,  $\theta_0 = 0.1$ ). Matching the peak time of the simulated light curve to  $t_{\text{obs,pk}} \approx 150$  days requires no significant time rescaling, and yields  $\alpha = t'_{\text{obs}}/t_{\text{obs}} \approx 1$ . Matching the peak flux to that observed requires equating Equation (6) to unity. Altogether, replacing the unprimed quantities by the best-fit values, and then making the rescaled

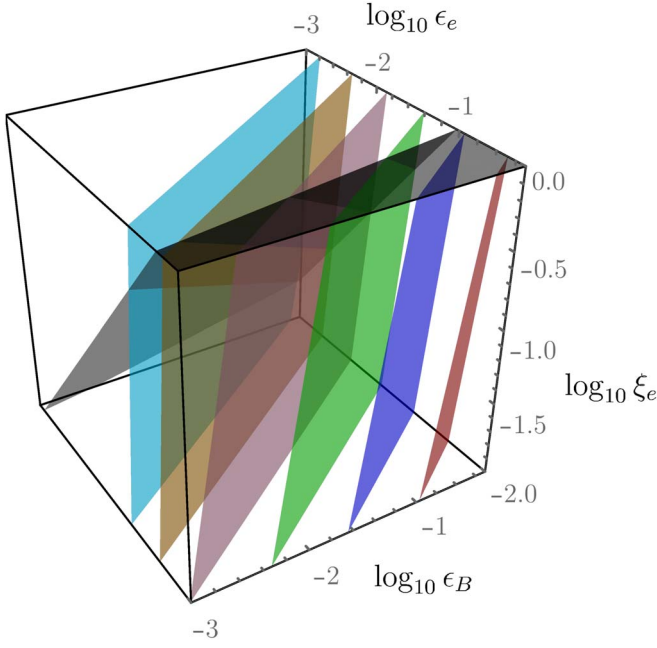


**Figure 3.** Allowed 3D parameter space  $[\xi_e, \epsilon_e, \epsilon_B]$  shown by planes in this space for different jet energies,  $\log_{10} E = 48.3, 48.6, \dots, 49.8$  (from red to cyan) following Equation (7), which is satisfied in the region above the black plane for which  $\xi_{e,\min} \leq \xi_e \leq 1$ . The constraint on  $\xi_{e,\min}$  from Equation (9) is shown by the black plane. The excluded region, for which  $\xi_{e,\min} > 1$ , is shown by the shaded transparent region on the top-face of the cube.

quantities unprimed, and solving for  $\zeta$ , yields

$$\zeta = \frac{E}{10^{50.4} \text{ erg}} = \frac{n}{10^{-3.6} \text{ cm}^{-3}} \approx \left( \frac{\epsilon_e}{10^{-1.8}} \right)^{\frac{4(1-p)}{(p+5)}} \left( \frac{\epsilon_B}{10^{-3.12}} \right)^{\frac{-(p+1)}{(p+5)}} \xi_e^{\frac{4(p-2)}{(p+5)}}, \quad (7)$$

where the equality in Equation (7) results from Equation (5) when  $\alpha = 1$ . This leaves us with a 3D allowed parameter space since we started with seven free model parameters ( $\theta_0 = 0.1$  was fixed by the simulation, leaving  $E, n, \epsilon_e, \epsilon_B, p, \xi_e, \theta_{\text{obs}}$ ) and used four observational constraints. The jet energy in Equation (7) decreases with increasing  $\epsilon_e, \epsilon_B$  and increases only weakly with  $\xi_e$ . A minimal energy constraint can be obtained by maximizing the values of  $\epsilon_e, \epsilon_B$  and minimizing that of  $\xi_e$ . This is demonstrated in Figure 3, where we show planes in the 3D parameter space  $[\xi_e, \epsilon_e, \epsilon_B]$  for different jet energies. Here we first use the fact that the broadband afterglow observations lie on a single PLS, with  $\nu > \nu_m$ , where we obtain

$$\nu_m = 8.93 \times 10^5 \xi_e^{-2} E_{k,\text{iso},52.7}^{1/2} \epsilon_{e,-1.8}^2 \epsilon_{B,-3.12}^{1/2} t_{\text{obs},150\text{d}}^{-3/2} \text{ Hz} \quad (8)$$

for  $t_{\text{obs},150\text{d}} = t_{\text{obs}}/(150 \text{ days})$  and  $p = 2.16$  from the expression for PLS G given in Granot & Sari (2002). This expression is only valid for a spherical flow and for an on-axis observer, for whom the flux is dominated by emission from material along the line of sight. At  $t_{\text{obs}} \geq t_{\text{obs,pk}} \approx 150$  days, the flux is dominated by that from the core of the jet with  $E_{k,\text{iso,c}} \lesssim 10^{52.7}$  erg. At  $t_{\text{obs}} < t_{\text{obs,pk}}$ , the flux is dominated by emission from material outside of the core at  $\theta > \theta_0$  with  $E_{k,\text{iso}} < E_{k,\text{iso,c}}$ . To obtain the value of  $\nu_m$  for an off-axis observer, we calibrated Equation (8) by comparing it with the value of  $\nu_m$  obtained from our numerical

simulation around the time of the earliest radio observations at  $t_{\text{obs}} \approx 16.4$  days. Next, we use the relation from Equation (7) in Equation (8) and replace  $E_{k,\text{iso}}$  to obtain an expression that depends only on shock microphysical parameters, which, for  $\nu_m(16.4 \text{ days}) < \nu_{\text{obs}} = 3$  GHz, yields a lower limit on  $\xi_e$

$$\xi_e > \xi_{e,\min} \approx 0.84 \epsilon_{e,-1}^{6/7} \epsilon_{B,-1}^{1/7}. \quad (9)$$

This constraint is shown as a shaded black plane in Figure 3 above which Equation (7) is satisfied. Another useful constraint here is that  $\xi_{e,\min} < 1$ , which yields

$$\epsilon_e < \epsilon_{e,\max} = 0.12 \epsilon_{B,-1}^{-1/6}. \quad (10)$$

We first use the constraint on  $\xi_e$  from Equation (9) in Equation (7) and remove the dependence on  $\xi_e$ . Next, we use the additional constraint on  $\epsilon_e$  from Equation (10) (which is equivalent to substituting  $\xi_e = 1$  and  $\epsilon_e = \epsilon_{e,\max}$  in Equation (7)) to obtain

$$E_{\min} \approx 7.7 \times 10^{48} \epsilon_{B,-1}^{-1/3} \text{ erg} = 5.3 \times 10^{48} \epsilon_{B,-0.5}^{-1/3} \text{ erg}, \quad (11)$$

as also demonstrated in Figure 3 by the intersection of the black plane with planes marked by jet energies  $E > E_{\min}$ .

If we consider only some  $\xi_e < 1$ , as may be expected on theoretical grounds, then Equation (9) will lead to  $\epsilon_{e,\max} = 0.12 \epsilon_{B,-1}^{-1/6} \xi_e^{7/6}$  and accordingly increase  $E_{\min}$  to

$$\begin{aligned} E_{\min} &\approx 3.6 \times 10^{49} \epsilon_{B,-1}^{-1/3} \xi_{e,-1}^{-2/3} \text{ erg} \\ &= 5.3 \times 10^{48} \epsilon_{B,-0.5}^{-1/3} \xi_e^{-2/3} \text{ erg}. \end{aligned} \quad (12)$$

Finally, according to Equation (7),  $E_{\min}$  also corresponds to a minimal CBM density,

$$\begin{aligned} n_{\min} &\approx 3.6 \times 10^{-5} \epsilon_{B,-1}^{-1/3} \xi_{e,-1}^{-2/3} \text{ cm}^{-3} \\ &= 5.3 \times 10^{-6} \epsilon_{B,-0.5}^{-1/3} \xi_e^{-2/3} \text{ cm}^{-3}. \end{aligned} \quad (13)$$

## 5. Model Comparison with Afterglow Image Size and Flux Centroid Motion

We compare the afterglow image size and flux centroid motion on the plane of the sky as obtained from our simulations to the GW170817/GRB 170817A radio observations. Very-long-baseline interferometry (VLBI) observations between 75 and 230 days revealed an unresolved source whose flux centroid showed apparent superluminal motion with  $\langle v_{\text{app}} \rangle / c = \langle \beta_{\text{app}} \rangle = 4.1 \pm 0.5$  (Mooley et al. 2018a). The flux centroid's location on the plane of the sky is defined as

$$\vec{r}_{\text{fc}} = (\tilde{x}_{\text{fc}}, \tilde{y}_{\text{fc}}) = \frac{\int dF_{\nu} \vec{r}}{\int dF_{\nu}} = \frac{\int d\tilde{x} d\tilde{y} I_{\nu} \vec{r}}{\int d\tilde{x} d\tilde{y} I_{\nu}}, \quad (14)$$

(e.g., Granot et al. 2018a), where  $dF_{\nu} = I_{\nu} d\Omega = I_{\nu} d_A^{-2} dS_{\perp}$ , with  $I_{\nu}$  being the specific intensity,  $d_A$  the angular distance, and  $dS_{\perp} = d\tilde{x} d\tilde{y}$  a transverse area element on the plane of the sky. The jet symmetry axis is in the  $\tilde{x}-\tilde{z}$  plane, where the  $\tilde{z}$ -axis points to the observer. Because of the flow's axisymmetry, the image has the reflection symmetry  $I_{\nu}(\tilde{x}, \tilde{y}) = I_{\nu}(\tilde{x}, -\tilde{y})$ . Therefore,  $\vec{r}_{\text{fc}} = (\tilde{x}_{\text{fc}}, 0)$  and the flux centroid moves along the  $\tilde{x}$ -axis. Since  $I_{\nu} = d_A^2 dF_{\nu} / dS_{\perp} \propto F_{\nu} / S_{\perp}$  where  $S_{\perp} \propto \ell^2$ , it

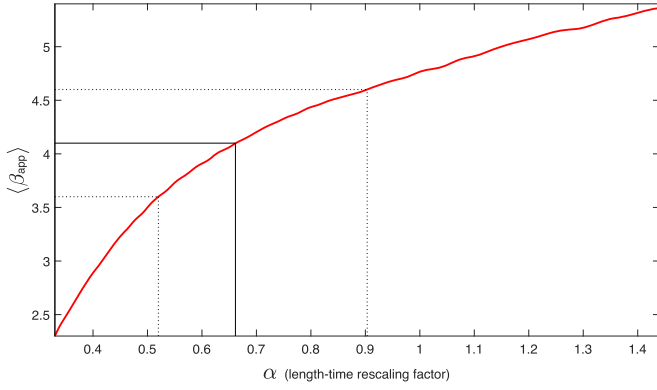


**Figure 4.** The observed mean radio flux centroid velocity between 75 and 230 days,  $\langle \beta_{\text{app}} \rangle = 4.1 \pm 0.5$  (horizontal lines; Mooley et al. 2018a), is compared to that from our best-fit simulation (thick red line) as a function of  $\alpha$ . It corresponds to  $\alpha = 0.661^{+0.242}_{-0.141}$  (vertical lines) or a  $1\sigma$  confidence interval  $0.520 < \alpha < 0.903$ .

scales in PLS G as  $\mathcal{I} = I'_{\nu,G}(t'_{\text{obs}}, \tilde{x}', \tilde{y}') / I_{\nu,G}(t_{\text{obs}}, \tilde{x}, \tilde{y})$ ,

$$\mathcal{I} = \zeta^{\frac{-(p+5)}{4}} \alpha^{\frac{-(3p+11)}{4}} \left( \frac{\epsilon'_e}{\epsilon_e} \right)^{p-1} \left( \frac{\epsilon'_B}{\epsilon_B} \right)^{\frac{p+1}{4}} \left( \frac{\xi'_e}{\xi_e} \right)^{2-p} \quad (15)$$

The image size, flux centroid location, and observed time all scale as  $\alpha = \tilde{x}'/\tilde{x} = \tilde{y}'/\tilde{y} = \tilde{x}'_{\text{fc}}/\tilde{x}_{\text{fc}} = t'_{\text{obs}}/t_{\text{obs}}$ , independent of the right side of Equation (15). The flux centroid's apparent velocity  $\beta_{\text{app}}$  remains unchanged, but shifts to the rescaled observer time (see, e.g., Section 4 of Granot et al. 2018a, for more details).

Figure 4 shows how our best-fit simulated  $\langle \beta_{\text{app}} \rangle$  varies with  $\alpha$ . The measured  $\langle \beta_{\text{app}} \rangle = 4.1 \pm 0.5$  corresponds to  $\alpha = 0.661^{+0.242}_{-0.141}$ , and is consistent (at the  $1.35\sigma$  level) with our fiducial model that fits the afterglow light curve ( $\alpha = 1$ ), which thus passes an important consistency check.

To calculate the afterglow image size and shape, we fit the surface brightness to an elliptical Gaussian,  $I_{\nu} \propto \exp[-(\tilde{x} - \tilde{x}_{\text{el}})^2/2\sigma_x^2 - \tilde{y}^2/2\sigma_y^2]$  centered at  $(\tilde{x}_{\text{el}}, 0)$ , where  $(\sigma_x, \sigma_y)$  are the standard deviations of the semimajor and semiminor axes along the  $\tilde{x}$ -axis and  $\tilde{y}$ -axis, respectively (Granot et al. 2018a). The top panel of Figure 5 shows the evolution of the afterglow flux-centroid location, and the afterglow image size and shape for  $\alpha = 1$  and for the  $\langle \beta_{\text{app}} \rangle$  best-fit  $\alpha = 0.661$ . Our image size is consistent with the upper limits from radio VLBI observations (Mooley et al. 2018a; Ghirlanda et al. 2019). The bottom panel of Figure 5 shows the flux centroid's location,  $\tilde{x}_{\text{fc}}(t_{\text{obs}})$ , as well as its instantaneous ( $\beta_{\text{app}} = |d\tilde{x}_{\text{fc}}/d(ct_{\text{obs}})|$ ) and mean ( $\langle \beta_{\text{app}} \rangle_0 = |\tilde{x}_{\text{fc}}|/ct_{\text{obs}}$ ) apparent velocities, for our fiducial model ( $\alpha = 1$ ), and over the  $1\sigma$  confidence interval of  $\alpha$  derived in Figure 4. We find that  $\beta_{\text{app}}(t_{\text{obs,pk}}) \approx \langle \beta_{\text{app}} \rangle$ .

The measured  $\langle \beta_{\text{app}} \rangle$  favors a slightly larger  $\theta_0$  compared to our  $\theta_0 = 0.1$ . The light-curve peak occurs when  $1/\Delta\theta \approx \Gamma(t_{\text{obs,pk}}) \approx \beta_{\text{app}}(t_{\text{obs,pk}}) \approx \langle \beta_{\text{app}} \rangle$ , implying  $\theta_0 \approx [(\beta_{\text{app}})(\theta_{\text{obs}}/\theta_0 - 1)]^{-1} \approx 0.116^{+0.016}_{-0.013}$  using the measured  $\langle \beta_{\text{app}} \rangle = 4.1 \pm 0.5$  and our inferred  $\theta_{\text{obs}}/\theta_0 = 3.1 \pm 0.1$ . The latter implies  $\Gamma(t_{\text{obs,pk}}) \propto \theta_0^{-1}$ , which in turn for the measured  $t_{\text{obs,pk}}(\theta_0) \approx 150$  days, and either pre- or post-jet break simple analytic dynamics, implies  $E/n \propto \theta_0^{-6}$ . This agrees with the best-fit values for our  $\theta_0 = 0.1, 0.2$  to within 34%,  $(0.2/0.1)^6(10^{50.32}/10^{-2})/(10^{50.4}/10^{-3.6}) \approx 1.337$ . Even for

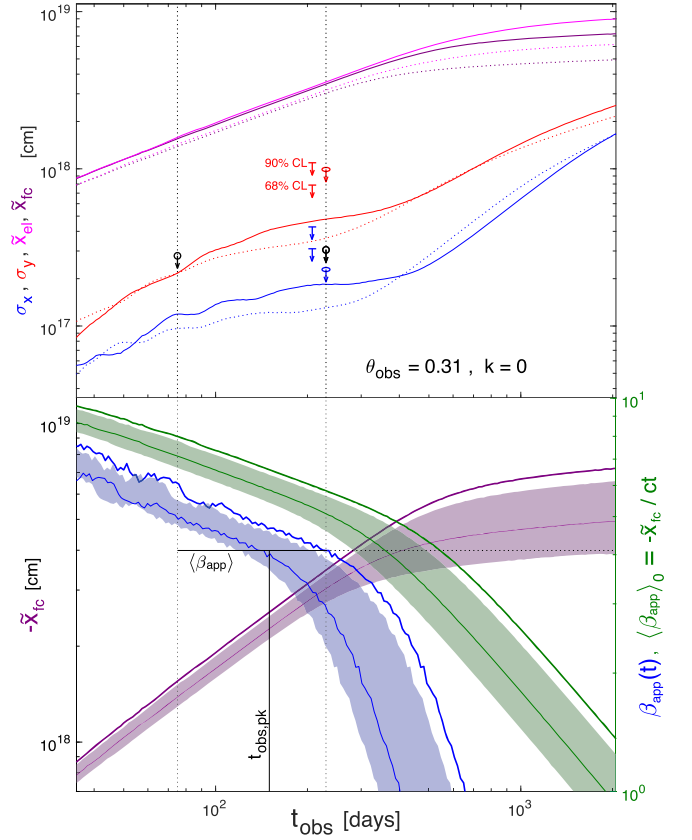


**Figure 5.** Top: the evolution of the afterglow image flux-centroid location ( $\tilde{x}_{\text{fc}}$ ; deep purple) and best-fit parameters to an elliptical Gaussian: semimajor axis  $\sigma_x$  (blue), semiminor axis  $\sigma_y$  (red), and center  $\tilde{x}_{\text{el}}$  (magenta). Solid lines are for our fiducial model, and dotted lines of the same color are for our best-fit length–time rescaling parameter  $\alpha = 0.661$ . Our model calculations are compared to observational upper limits on the semimajor (red) and semiminor (blue). The limits at 75, 230 days (Mooley et al. 2018a) are  $\sim 1\sigma$ ; ellipse symbols assume a 4:1 axis ratio; black-circle symbols assume a circular Gaussian and apply to both axes. At 207 days (Ghirlanda et al. 2019) we show 68% confidence level and 90% confidence level limits for our calculated axis ratio ( $\sigma_y/\sigma_x = 2.55$ ). The vertical dotted black lines indicate the two epochs (75 and 230 days) between which  $\langle \beta_{\text{app}} \rangle = 4.1 \pm 0.5$  was measured (Mooley et al. 2018a). Bottom: the evolution of the flux-centroid location (left y-axis) for our fiducial model (deep purple) and its rescaled version to best fit the measured  $\langle \beta_{\text{app}} \rangle$  (shaded region of matching color for the  $1\sigma$  confidence region), as well as of the flux centroid's apparent velocity (right y-axis). For the latter we show both the mean apparent velocity from  $t = 0$ ,  $\langle \beta_{\text{app}} \rangle_0 = |\tilde{x}_{\text{fc}}|/ct_{\text{obs}}$  (dark green), and for the instantaneous  $\beta_{\text{app}} = |d\tilde{x}_{\text{fc}}/d(ct_{\text{obs}})|$  (blue).

$\theta_0 = 0.2$ , a derivation of  $E_{\text{min}}$  following the one done above for  $\theta_0 = 0.1$  gives a result very similar to Equation (11), implying that it is quite robust. Altogether,  $\langle \beta_{\text{app}} \rangle$  provides an additional observational constraint that allows us to constrain an additional model parameter,  $\theta_0$ , which still leaves us with a 3D allowed parameter space.

## 6. Discussion and Conclusions

This work demonstrates using afterglow light curves and image size, shape, and flux centroid motion, all derived from 2D hydrodynamical numerical simulations, that an initially THJ can broadly fit the afterglow observations of GW170817/GW170817A for  $\theta_0 \approx 0.1$  and  $\theta_{\text{obs}}/\theta_0 \approx 3$  at  $t_{\text{obs}} \gtrsim t_{\text{obs,pk}}$ . We show that simulations of initially THJs with a modest  $\Gamma_0 \sim 20\text{--}25$  can only be used to fit the late-time observations

near the light curve's peak at  $t_{\text{obs,pk}} \approx 150$  days. Fitting earlier observations at  $t_{\text{obs}} \lesssim 60$  days requires  $\Gamma_0 \gtrsim 25$ .

We analytically express the allowed parameter space (Equations (7)) showing the full degeneracies between the model parameters, and find a robust lower limit on the jet's true energy,  $E_{\text{min}} \approx 5.3 \times 10^{48}$  erg (Equation (11)), and the CBM density,  $n_{\text{min}} \approx 5.3 \times 10^{-6} \text{ cm}^{-3}$  (Equation (13)).

Our numerical simulations are initialized using a conical wedge from the BM76 self-similar solution; a similar setup is used in the BOXFITv2 code. The simulation is initialized at a finite lab-frame time  $t_0 = t(\Gamma_0)$  corresponding to the modest  $\Gamma_0 = \Gamma(t_0)$ . Therefore, no flux contributions are obtained from the simulated region at  $t < t_0 \Leftrightarrow t_{\text{obs}} < t_{\text{obs},0}$ . Artificially supplementing the light curve at those times with flux arising from the initial condition (a THJ) over a wide time-range produces an early sharply rising flux for an off-axis ( $\theta_{\text{obs}} > \theta_0$ ) observer. However, within a dynamical time ( $t_0 < t \lesssim 2t_0 \Leftrightarrow t_{\text{obs},0} < t_{\text{obs}} \lesssim 2t_{\text{obs},0}$ ), as the outflow relaxes from the initial conditions it develops a bow-shock like angular structure that resembles a structured jet having an energetic relativistic core surrounded by mildly (and sub-) relativistic low-energy material. Outside the highly relativistic core, whose emission is strongly beamed, the slower material makes the dominant contribution to the flux for off-axis observers due to its much wider beaming cone. As the jet's core decelerates, its beaming cone widens and the observer sees a gradual rise in flux until the entire core becomes visible, at which point the flux peaks and starts to decline thereafter, gradually joining the on-axis light curve.

We demonstrate here that by using increasingly larger  $\Gamma_0 = 20, 40, 60$  the initial observed time can be shifted to correspondingly earlier times,  $t_{\text{obs},0} = 38.1, 23.0, 18.3$  days, thereby replacing the sharp rise in flux with a much more gradual rise. In GRB 170817A, the shallow flux rise seen from  $t_{\text{obs},0} \simeq 10$  days can potentially be reproduced for  $\Gamma_0 \gtrsim 10^{2.5}$ , which are physically plausible but computationally challenging, although the exact shape of the early rising light curve in this case is still unclear. Nevertheless, the initially THJ model has some limitations. For example, the early time afterglow light curve shows a power-law rise ( $F_\nu \propto t_{\text{obs}}^{0.8}$ ) to the peak, whereas the model light curve has some curvature. In this work we did not carry out a detailed model fit to the data to determine the goodness of fit since our simulations were limited to  $\Gamma_0 = 60$  and could not fit observations at  $t_{\text{obs}} \lesssim 40$  days. Numerical simulations of structured jets that show a greater degree of complexity, and therefore are more realistic, also have larger number of model parameters, which allows them to capture the subtleties of the observed afterglow data more effectively.

Numerical simulations of a relativistic jet penetrating through the dynamical ejecta/neutrino-driven wind of a binary neutron star merger (Bromberg et al. 2018; Gottlieb et al. 2018; Xie et al. 2018; Geng et al. 2019) find that the emergent jet develops a core-dominated angular structure broadly similar to what we find. Moreover, our afterglow model fit parameters are consistent with works featuring initially structured core-dominated jets. This makes it hard to distinguish between both scenarios from afterglow observations alone, particularly close to and after the peak time of the light curve (also see, e.g., Gottlieb et al. 2019) when emission from the core starts dominating the observed flux, thereby validating the use of initially THJ simulations as an attractive tool for afterglow modeling of core-dominated jets.

Both the jet's dynamics and initial angular structure outside its core, before it is decelerated by the external medium, affects the afterglow emission before the light-curve peak time. From the afterglow observations alone, it might be difficult to disentangle their effects, however, they may be better probed by the prompt emission. For example, in the case of GRB 170817A, its highly subluminal and mildly soft prompt  $\gamma$ -ray emission rules out an initial THJ (e.g., Abbott et al. 2017b; Granot et al. 2017), favoring instead emission from sub-energetic mildly relativistic material near our line of sight.

R.G. and J. G. are supported by the Israeli Science Foundation under grant No. 719/14. F.D.C. acknowledges support from the UNAM-PAPIIT grant IN117917. We acknowledge the support from the Miztli-UNAM supercomputer (project LANCAD-UNAM-DGTIC-281) in which the simulations were performed.

### ORCID iDs

Ramandeep Gill  <https://orcid.org/0000-0003-0516-2968>  
Jonathan Granot  <https://orcid.org/0000-0001-8530-8941>  
Fabio De Colle  <https://orcid.org/0000-0002-3137-4633>

### References

- Abbott, B. P., Abbott, R., Abbott, T. D., et al. 2017a, *PhRvL*, **119**, 161101  
Abbott, B. P., Abbott, R., Abbott, T. D., et al. 2017b, *ApJL*, **848**, L13  
Abbott, B. P., Abbott, R., Abbott, T. D., et al. 2017c, *ApJL*, **848**, L12  
Bietenholz, M. F., De Colle, F., Granot, J., Bartel, N., & Soderberg, A. M. 2014, *MNRAS*, **440**, 821  
Blandford, R. D., & McKee, C. F. 1976, *PhFl*, **19**, 1130  
Bromberg, O., Tchekhovskoy, A., Gottlieb, O., Nakar, E., & Piran, T. 2018, *MNRAS*, **475**, 2971  
Coulter, D. A., Foley, R. J., Kilpatrick, C. D., et al. 2017, *Sci*, **358**, 1556  
D'Avanzo, P., Campana, S., Salafia, O. S., et al. 2018, *A&A*, **613**, L1  
De Colle, F., Granot, J., López-Cámara, D., & Ramirez-Ruiz, E. 2012a, *ApJ*, **746**, 122  
De Colle, F., Ramirez-Ruiz, E., Granot, J., & Lopez-Camara, D. 2012b, *ApJ*, **751**, 57  
Dobie, D., Kaplan, D. L., Murphy, T., et al. 2018, *ApJL*, **858**, L15  
Eichler, D., & Granot, J. 2006, *ApJL*, **641**, L5  
Eichler, D., & Waxman, E. 2005, *ApJ*, **627**, 861  
Geng, J.-J., Zhang, B., Kölligan, A., Kuiper, R., & Huang, Y.-F. 2019, *ApJL*, **877**, L40  
Ghirlanda, G., Salafia, O. S., Paragi, Z., et al. 2019, *Sci*, doi:10.1126/science.aau8815  
Gill, R., & Granot, J. 2018, *MNRAS*, **478**, 4128  
Gottlieb, O., Nakar, E., & Piran, T. 2018, *MNRAS*, **473**, 576  
Gottlieb, O., Nakar, E., & Piran, T. 2019, *MNRAS*, **488**, 2405  
Granot, J. 2005, *ApJ*, **631**, 1022  
Granot, J. 2007, *RMxAC*, **27**, 140  
Granot, J. 2012, *MNRAS*, **421**, 2610  
Granot, J., De Colle, F., & Ramirez-Ruiz, E. 2018a, *MNRAS*, **481**, 2711  
Granot, J., Gill, R., Guetta, D., & De Colle, F. 2018b, *MNRAS*, **481**, 1597  
Granot, J., Guetta, D., & Gill, R. 2017, *ApJL*, **850**, L24  
Granot, J., Miller, M., Piran, T., Suen, W. M., & Hughes, P. A. 2001, in *Gamma-ray Bursts in the Afterglow Era*, ed. E. Costa, F. Frontera, & J. Hjorth (Berlin: Springer), 312  
Granot, J., Panaitescu, A., Kumar, P., & Woosley, S. E. 2002, *ApJL*, **570**, L61  
Granot, J., Piran, T., & Sari, R. 1999, *ApJ*, **513**, 679  
Granot, J., & Ramirez-Ruiz, E. 2012, in *Gamma-ray Bursts*, ed. C. Kouveliotou et al. (Cambridge: Cambridge Univ. Press), 215  
Granot, J., & Sari, R. 2002, *ApJ*, **568**, 820  
Haggard, D., Nynka, M., & Ruan, J. J. 2018, GCN, 23137, 1  
Hajela, A., Margutti, R., Fong, W., et al. 2019, GCN, 24000, 1  
Hallinan, G., Corsi, A., Mooley, K. P., et al. 2017, *Sci*, **358**, 1579  
Lamb, G. P., & Kobayashi, S. 2018, *MNRAS*, **478**, 733  
Lazzati, D., Perma, R., Morsony, B. J., et al. 2018, *PhRvL*, **120**, 241103  
Lithwick, Y., & Sari, R. 2001, *ApJ*, **555**, 540

- Margutti, R., Alexander, K. D., Xie, X., et al. 2018, [ApJL](#), **856**, L18
- Mooley, K. P., Deller, A. T., Gottlieb, O., et al. 2018a, [Natur](#), **561**, 355
- Mooley, K. P., Nakar, E., Hotokezaka, K., et al. 2018b, [Natur](#), **554**, 207
- Nakar, E., & Piran, T. 2018, [MNRAS](#), **478**, 407
- Resmi, L., Schulze, S., Ishwara-Chandra, C. H., et al. 2018, [ApJ](#), **867**, 57
- Salmonson, J. D. 2003, [ApJ](#), **592**, 1002
- Sari, R., Piran, T., & Narayan, R. 1998, [ApJL](#), **497**, L17
- Troja, E., Piro, L., Ryan, G., et al. 2018, [MNRAS](#), **478**, L18
- Troja, E., Piro, L., van Eerten, H., et al. 2017, [Natur](#), **551**, 71
- Troja, E., van Eerten, H., Ryan, G., et al. 2018, [MNRAS](#), in press, (arXiv:1808.06617)
- van Eerten, H., & MacFadyen, A. 2013, [ApJ](#), **767**, 141
- van Eerten, H., van der Horst, A., & MacFadyen, A. 2012, [ApJ](#), **749**, 44
- van Eerten, H. J., & MacFadyen, A. I. 2011, [ApJL](#), **733**, L37
- van Eerten, H. J., & MacFadyen, A. I. 2012, [ApJL](#), **747**, L30
- Xie, X., Zrake, J., & MacFadyen, A. 2018, [ApJ](#), **863**, 58